



## Characterization of sodium ion electrochemical reaction with tin anodes: Experiment and theory

Loïc Baggetto<sup>a,\*</sup>, P. Ganesh<sup>b</sup>, Roberta P. Meisner<sup>a,c</sup>, Raymond R. Unocic<sup>a</sup>, Jean-Claude Jumas<sup>d</sup>, Craig A. Bridges<sup>e</sup>, Gabriel M. Veith<sup>a,\*</sup>

<sup>a</sup> Materials Science and Technology Division, Oak Ridge National Laboratory, 1 Bethel Valley Rd., Oak Ridge, TN 37831, USA

<sup>b</sup> Center for Nanophase Materials Sciences, Oak Ridge National Laboratory, 1 Bethel Valley Rd., Oak Ridge, TN 37831, USA

<sup>c</sup> Department of Materials Science and Engineering, University of Tennessee Knoxville, Knoxville, TN 37996, USA

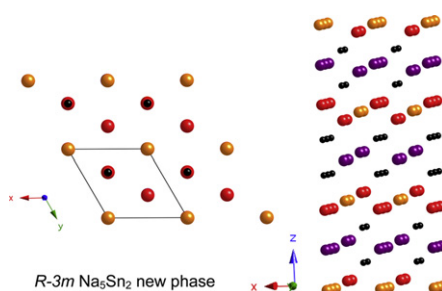
<sup>d</sup> Institut Charles Gerhardt, Université Montpellier II 34095 Montpellier Cedex 5, France

<sup>e</sup> Chemical Sciences Division, Oak Ridge National Laboratory, 1 Bethel Valley Rd., Oak Ridge, TN 37831, USA

### HIGHLIGHTS

- Bulk structure of Na–Sn studied by XRD, DFT and Mössbauer spectroscopy.
- Identification of new *R*-3*m* phase of composition Na<sub>5</sub>Sn<sub>2</sub>.
- Surface chemistry probed by XPS as a function of Na content.
- Catalytic decomposition of electrolyte caused by Sn<sup>4+</sup> and not metallic Sn.

### GRAPHICAL ABSTRACT



### ARTICLE INFO

#### Article history:

Received 9 November 2012

Received in revised form

14 January 2013

Accepted 16 January 2013

Available online 29 January 2013

#### Keywords:

Sodium ion reaction of Sn anodes  
Na<sub>5</sub>Sn<sub>2</sub> (*R*-3*m*) metastable phase (XRD-  
TEM-SAED)

Phase predictions (DFT)

<sup>119</sup>Sn Mössbauer spectroscopy

Surface chemistry (XPS)

### ABSTRACT

Tin anodes show a rich structure and reaction chemistry which we have investigated in detail. Upon discharge five plateaus are observed corresponding to  $\beta$ -Sn, an unidentified phase (Na/Sn = 0.6), an amorphous phase (Na/Sn = 1.2), a hexagonal *R*-3*m* Na<sub>5</sub>Sn<sub>2</sub>, and fully sodiated *I*-43*d* Na<sub>15</sub>Sn<sub>4</sub>. With charging there are six plateaus related to the formation of Na<sub>5</sub>Sn<sub>2</sub> followed by the formation of amorphous phases and  $\beta$ -Sn. Upon cycling the formation of metastable Na<sub>5</sub>Sn<sub>2</sub> seems to be suppressed.

Theoretical voltages calculated from existing crystal structures using DFT provide a good match with constant current and quasi-equilibrium measurements (GITT). Search for additional (meta)stable phases using cluster-expansion method predicts many phases lower in energy than the convex hull obtained from known structures, including the *R*-3*m* Na<sub>5</sub>Sn<sub>2</sub> phase. The presence of multiple phases in varying lattices with similar formation energy suggests why the reaction mechanism is non-reversible. <sup>119</sup>Sn Mössbauer spectroscopy results indicate a decrease of the isomer shift with increasing Na/Sn content, which is less pronounced than for Li–Sn compounds likely due to the lower electropositivity of Na.

The electrode surface is terminated with an SEI layer rich in carbonates (Na<sub>2</sub>CO<sub>3</sub> and Na CO<sub>3</sub>R) as evidenced by XPS. After charge at 2 V, strong evidence for the formation of oxidized Sn<sup>4+</sup> is obtained. Subjecting the electrode to a rest after charge at 2 V reveals that aging in the electrolyte reduces the oxidized Sn<sup>4+</sup> into Sn<sup>2+</sup> and Sn<sup>0</sup>, and concomitantly suppresses the electrolyte decomposition represented by an anomalous discharge plateau at 1.2 V. Thereby, the catalytic decomposition of the electrolyte during discharge is caused by nanosized Sn particles covered by oxidized Sn<sup>4+</sup> and not by pure metallic Sn.

© 2013 Elsevier B.V. All rights reserved.

\* Corresponding authors. Tel./fax: +1 865 241 6126.

E-mail addresses: [baggettol@ornl.gov](mailto:baggettol@ornl.gov) (L. Baggetto), [veithgm@ornl.gov](mailto:veithgm@ornl.gov) (G.M. Veith).

## 1. Introduction

Alternative energy storage systems to lithium-ion technology are attracting increasing attention in the field of rechargeable batteries [1,2]. Sodium is widely abundant, cheap and has a  $\text{Na}/\text{Na}^+$  redox potential around 0.3 V above that of  $\text{Li}/\text{Li}^+$ , which renders Na a promising candidate as a sustainable alternative to current Li-ion battery technologies. Despite the growing interest in rechargeable Na-ion batteries there has been relatively little exploration of anode materials compared to cathode materials [1–3]. Studies of anode materials have primarily been phenomenological lacking in-depth understanding of bulk and interface chemistries. Of notable exception have been the investigation of  $\text{Na}_2\text{Ti}_3\text{O}_7$  [4] and Density Functional Theory (DFT) predictions of reaction potentials for several Na-alloying anode materials [5].

Among the various group-IVA candidates from the table of periodic elements (C, Si, Ge, Sn and Pb), Sn appears to be the most promising from the perspectives of both high storage capacity and low voltage operation [5]. Indeed, the theoretical capacity of Sn is about  $847 \text{ mAh g}^{-1}$  when assuming the full conversion into  $\text{Na}_{15}\text{Sn}_4$ . Based on this high potential capacity Sn/C and SnSb/C electrodes were investigated and characterized as high-storage capacity anodes for Na, however the reaction mechanism was not studied [6,7]. The fully sodiated  $\text{Na}_{15}\text{Sn}_4$  phase was evidenced during the electrochemical reaction of Sn by Komaba et al., thus confirming the potential for Sn as a high storage capacity anode [8]. More recently, Ellis et al. investigated the phase transformations of sputtered Sn films during Na-ion electrochemical reaction by means of *in situ* X-ray diffraction (XRD) [9]. Their main findings are the presence of four bi-phasic plateaus corresponding to three unknown phases and to cubic  $\text{Na}_{15}\text{Sn}_4$  as the fully sodiated compound. The current work moves beyond a cursory investigation of the anode and develops a fundamental understanding of the bulk and surface chemistry of Sn anodes.

The present study employs model thin-films of Sn, with various thicknesses, for investigating the electrochemical behavior of the Na–Sn system. By means of constant current cycling using different cycling cut-off voltages we describe more precisely the conjugation of reactions occurring during (de)sodiation. Using the Galvanostatic Intermittent Titration Technique (GITT), we approach more accurately the reaction thermodynamics and correlate our findings with the potential profile predicted from DFT calculations. The fundamental structural changes occurring in the bulk have been investigated by means of XRD, DFT and Mössbauer Spectroscopy. Moreover, transmission electron microscopy (TEM) and selected area electron diffraction (SAED) have been used to aid in the identification of unknown phases. Finally, we have studied the evolution of the surface chemistry (oxidation states of Sn and solid electrolyte interphase (SEI) chemistry), which is found to dictate the electrode stability [9,10], by means of X-ray photoelectron spectroscopy (XPS). These combined results offer a much clearer description of the electrochemical reaction when compared to recently published data [6–9]. For instance we report the existence of additional plateaus during both discharge and charge. More importantly, we disclose the identification of a new metastable phase in the Na–Sn system of nominal composition  $\text{Na}_5\text{Sn}_2$  with hexagonal structure and  $R\text{-}3m$  space group. Our preliminary computational structure search using cluster-expansion based methods reveal additional phases for  $\text{Na}/\text{Sn} \leq 2.5$ , which prompts for a more detailed investigation of kinetic pathways that not only involve ground-state phases, but also metastable phases. Finally, the role of surface oxides obtained after charging at 2 V is explained in relation with the catalytic decomposition of the electrolyte during the subsequent discharge.

## 2. Experimental

### 2.1. Samples preparation

Sn films of various thicknesses (50 nm–6  $\mu\text{m}$ ) were prepared onto roughened Cu foils using DC magnetron sputtering in a chamber with a base pressure below  $7 \cdot 10^{-7}$  Torr. Ultra high purity Sn (99.999%, Kurt J. Lesker) and Ar (99.99%, Air Liquide) were used as target material and sputtering gas at 20 mTorr deposition pressure and 20 W DC power. For XRD and XPS identifications,  $\text{SnO}_2$  films were prepared using an Ar/ $\text{O}_2$  (20/10) mixture. Thickness was monitored using a quartz microbalance installed inside the chamber. The weight of thick films was measured on a Mettler MT5 balance with 1  $\mu\text{g}$  precision, which represents less than 0.1% the weight of thick electrodes used for the accurate Na/Sn content determination. After preparation, the thin film samples were stored inside an Ar-filled glovebox.

### 2.2. Experimental characterization

Electrochemical characterization was conducted at 25 °C inside a thermostated incubator using 2-electrode coin cells (2032 hardware) prepared inside an Ar-filled glovebox. The cells consisted of pure Na as counter electrode, two pieces of glass fiber separator impregnated by 1 M  $\text{NaClO}_4$  in Propylene Carbonate (PC) electrolyte solution. Galvanostatic cycling was performed on a Maccor 4000 series between 0.005 and 2 V vs.  $\text{Na}/\text{Na}^+$  for electrodes with a diameter of 1.27 cm diameter (surface area of  $1.267 \text{ cm}^2$ ). The corresponding currents are given in the figures. The charge (Na-ion extraction, desodiation) cut-off was varied at 0.4, 0.6, 0.7, 1.3, 1.6 and 2 V and the discharge (Na-ion insertion, sodiation) cut-off was set at 60 and 5 mV to investigate the reversibility of the electrochemical reaction. Capacities are expressed in  $\mu\text{Ah}$  per  $\text{cm}^2$  footprint area per  $\mu\text{m}$  anode thickness ( $\mu\text{Ah cm}^{-2} \mu\text{m}^{-1}$ ) or in  $\text{mAh g}^{-1}$  for electrodes weighted on the microbalance. GITT discharge was measured during the second cycle on electrodes cycled between 0.005 and 0.7 V during the first cycle, and GITT charge was acquired during the first cycle. Rest periods were set at 3 h for a total of 100–150 points of measurement per single charge or discharge, requiring 1000 h of GITT measurement per cycle. After electrochemical preparation, samples were prepared for the various characterizations inside an Ar-filled glovebox. For XPS and TEM characterization, specimens were extracted from coin cells and rinsed with anhydrous dimethyl carbonate (DMC). For XRD and Mössbauer spectroscopy characterizations, samples were extracted from coin cells and the excess of electrolyte was removed by pressing onto a fiber paper.

XRD scans were acquired on two diffractometers. A Scintag Pad V diffractometer equipped with  $\text{Cu K}\alpha$  radiation was used for *ex situ* measurements of thin film samples sealed inside a homemade coin cell equipped with a Kapton window sealed with vacuum epoxy resin. A Panalytical Xpert diffractometer equipped with  $\text{Mo K}\alpha$  radiation and X'Celerator detector was used for *ex situ* measurements on samples sealed with Kapton tape (25 or 50  $\mu\text{m}$ ) onto a glass slide. The scans measured on the Panalytical used  $\frac{1}{4}^\circ$  fixed slits and  $\frac{1}{2}^\circ$  anti-scatter slit. The small beam overflow induced at low angles was corrected on corresponding scans using the method described by Krüger and Fischer [10]. Samples were brought to the diffractometer inside an Ar-filled pouch bag prepared inside the glovebox and opened at the last moment. Scans were limited to no more than 80 min on the Scintag and 45 min on the Panalytical, to limit X-ray exposure and the possible reaction of the samples with moisture, which was also found by others to be critical [9]. For every reported position on the electrochemical curve, at least two samples were prepared for XRD characterization, thereby ensuring a good

reproducibility of measurement. A reference Sn powder (Sigma–Aldrich) was measured on Cu  $K_{\alpha}$  for reference. Crystal structures for Li–Sn and Na–Sn compounds were obtained from the ICSD database.

TEM characterization was performed using a Hitachi HF3300 S/TEM instrument operating at 300 kV. The electrode material was scraped onto a lacey carbon Cu TEM grid then transferred to the microscope using an air-tight transfer holder. Bright field TEM imaging was used to image the electrode nanoparticles while selected area electron diffraction (SAED) was used to support the crystal structure parameters found by XRD.

Surface chemistry was probed using a PHI 3056 XPS spectrometer equipped with Al  $K_{\alpha}$  and Mg  $K_{\alpha}$  sources (1486.6 and 1253.6 eV) at a measurement pressure below  $10^{-8}$  Torr. After electrochemical preparation, within half hour electrodes were disassembled in an Ar glovebox and rinsed with anhydrous DMC using a small volume (less than 0.5 mL). Next, samples were transferred to the XPS chamber using an air-tight vacuum transfer system. High resolution scans were acquired at 350 W with 23.5 eV pass energy and 0.05 eV energy step. Survey scans were measured at 350 W with 93.9 eV pass energy and 0.3 eV energy step. The binding energies were shifted by setting the adventitious carbon signal to 284.8 eV to account for charging. The intensities of the presented spectra are not normalized and are simply shifted vertically for clarity. The spectra were deconvoluted using Gaussian–Lorentzian functions and a Shirley-type background. Powders of  $\text{Na}_2\text{CO}_3$  and  $\text{NaClO}_4$  (Sigma–Aldrich) were measured as references.

$^{119}\text{Sn}$  transmission Mössbauer spectroscopy was acquired at room temperature in the constant acceleration mode using components manufactured by ORTEC and WissEl. The source used for these experiments was  $^{119m}\text{Sn}$  embedded in a  $\text{CaSnO}_3$  matrix. The velocity scale was calibrated with the magnetic sextet of a high-purity iron foil as the reference absorber, and  $^{57}\text{Co}$  (Rh) was used as the source. The spectra were fitted to Gauss–Lorentzian profiles by the least-squares method. All isomer shifts are given with respect to the room temperature spectrum of  $\text{BaSnO}_3$ . The maximum experimental error on hyperfine parameters is estimated to be  $\pm 0.05 \text{ mm s}^{-1}$ .

### 2.3. Computational methods

All first-principles total energy calculations were performed using a Perdew–Burke–Ernzerhof generalized gradient approximation (PBE–GGA) and a projector-augmented-wave (PAW) potential as implemented in VASP [11–13]. Voltages were computed using known structures from the ICSD using the two-phase coexistence method [14] of calculating average voltages with a Na body centered cubic metal as the reference electrode:

$$V(x) = [E(\text{Na}_x\text{Sn}) - E(\text{Na}_{x+\Delta x}\text{Sn})]/\Delta x + E^{\text{BCC}}(\text{Na}) \quad (1)$$

for  $x = \text{Na/Sn}$  concentration and ‘ $E$ ’ is the first-principles total energy calculated at the experimental lattice parameter with atomic relaxations. The average voltage should be close to the thermodynamic equilibrium voltages from experiments, but depends on the proper identification of the coexisting phases. For atomic relaxation, forces were relaxed down to  $0.001 \text{ eV } \text{\AA}^{-1}$ . A plane-wave cutoff of 500 eV was used with sufficient number of  $\mathbf{k}$ -points to achieve energy convergence down to 10 meV/unit cell. In addition, to perform alloy thermodynamics, first-principles total energies were used to parameterize a cluster expansion (i.e. an effective Hamiltonian) describing the total energy of the  $\text{Na}_x\text{Sn}$  alloy in terms of the configurational degrees of freedom

[15,16]. The binary alloy was modeled as a substitutional alloy starting with the Sn-host structure in various crystal lattices. In this paper we present results from the following Sn-host structures:  $Fm-3m$  (fcc),  $P6_3/mmc$  (hcp),  $Pmma$  (orthorhombic),  $R-3m$  (rhombohedral),  $I4_1/amd$  (body-centered tetragonal) (coordinates of the Sn-host are given in the Supplementary section). The MAPS program as implemented in ATAT package [16,17] was used to perform the structure search over the entire composition range and fit the effective cluster expansion interaction parameters. Clusters up to four points (i.e. sites) were included in the fit, and the quality of the fit was measured using a cross validation score [16,17] that predicts the quality of the cluster expansion in predicting energies of structures not included in the fit. The first-principles calculations performed to obtain the fit employed full lattice relaxations with EDIFFG =  $-0.001$  in the VASP INCAR file. Cross validation scores were less than 0.25 for all fits in the entire composition range, and were less than 0.05 in compositions 0 to 0.5 in Na content. Formation energies were calculated using the  $\beta$ -Sn and the  $\beta$ -Na pure phases as the reference:

$$F(\text{Na}_a\text{Sn}_b) = E(\text{Na}_a\text{Sn}_b)/\text{atom} - aE(\beta\text{-Na})/\text{atom} - bE(\beta\text{-Sn})/\text{atom} \quad (2)$$

A more thorough study using the cluster-expansion method and presently discovered metastable/stable phases to obtain the temperature-composition phase diagram will be presented in the near future.

## 3. Results and discussion

### 3.1. Electrochemical characterization

The starting Sn and  $\text{SnO}_2$  thin film materials were characterized by XRD, Fig. S1.  $\text{SnO}_2$  was prepared and characterized by XRD in order to help in the characterization of the surface oxides (see Section 3.4). Both materials are single phase with lattice parameters close to those expected for the bulk  $\beta$ -Sn and cassiterite (rutile)  $\text{SnO}_2$  materials, respectively (see Table 1). The typical potential profiles obtained on thick (2  $\mu\text{m}$ ) and thin (100 nm) Sn thin film electrodes are presented in Fig. 1a and b, respectively. The use of a microbalance with  $\mu\text{g}$  precision allows for a more accurate determination of the Na/Sn content within the thick electrodes. Thick electrodes, however, suffer from sluggish kinetics, likely caused by Na-ion solid-state diffusion, which thereby necessitate the use of very low currents of typically C/100 or less.

**Table 1**

Structural data of the Na–Sn electrochemical phases. Lattice parameters  $a$ ,  $b$ ,  $c$  (Å) are obtained from Rietveld refinements of the XRD spectra.

Material	Structure	$a$	$b$	$c$
Pristine $\beta$ -Sn powder	Tetragonal ( $I4_1/amd$ )	5.830	5.830	3.181
Pristine $\beta$ -Sn films	Tetragonal ( $I4_1/amd$ )	5.832	5.832	3.182
$\text{Na}_x\text{Sn}$ (discharge 0.46 V)	$\beta$ -Sn Tetragonal ( $I4_1/amd$ )	5.829	5.829	3.180
$\text{Na}_x\text{Sn}$ (discharge 0.22 V)	Unknown	?	?	?
$\text{Na}_x\text{Sn}$ (discharge 0.12 V)	Amorphous/nanocrystalline	–	–	–
$\text{Na}_x\text{Sn}$ (discharge 0.06 V)	$\text{Na}_5\text{Sn}_2$ ( $R-3m$ )	5.397	5.397	22.257
$\text{Na}_5\text{Sn}_2$ (DFT prediction)	$\text{Na}_5\text{Sn}_2$ ( $R-3m$ )	5.454	5.454	22.619
$\text{Na}_x\text{Sn}$ (discharge 0.06 V)	$\text{Na}_5\text{Sn}_2$ ( $C2/m$ ), $\beta = 112.39^\circ$	9.374	5.380	8.024
$\text{Na}_5\text{Sn}_2$ (DFT prediction)	$\text{Na}_5\text{Sn}_2$ ( $C2/m$ ) $\beta = 112.65^\circ$	9.446	5.455	8.170
$\text{Na}_{15}\text{Sn}_4$ (discharge 0 V)	Cubic ( $I-43d$ )	13.175	13.175	13.175
$\text{Na}_x\text{Sn}$ (charge 0.2 V)	$\text{Na}_5\text{Sn}_2$ ( $R-3m$ )	5.416	5.416	22.377
$\text{Na}_x\text{Sn}$ (charge 0.4 V)	Amorphous	–	–	–
$\text{Na}_x\text{Sn}$ (charge 0.6 V)	Amorphous + $\beta$ -Sn	–	–	–
$\text{Na}_x\text{Sn}$ (charge 0.7 V)	Amorphous + $\beta$ -Sn	5.822	5.822	3.177
Pristine cassiterite $\text{SnO}_2$	Tetragonal ( $P4_2/mnm$ )	4.743	4.743	3.185
$\text{Na}_x\text{SnO}_2$ (discharge 0 V)	Amorphous/nanocrystalline	–	–	–

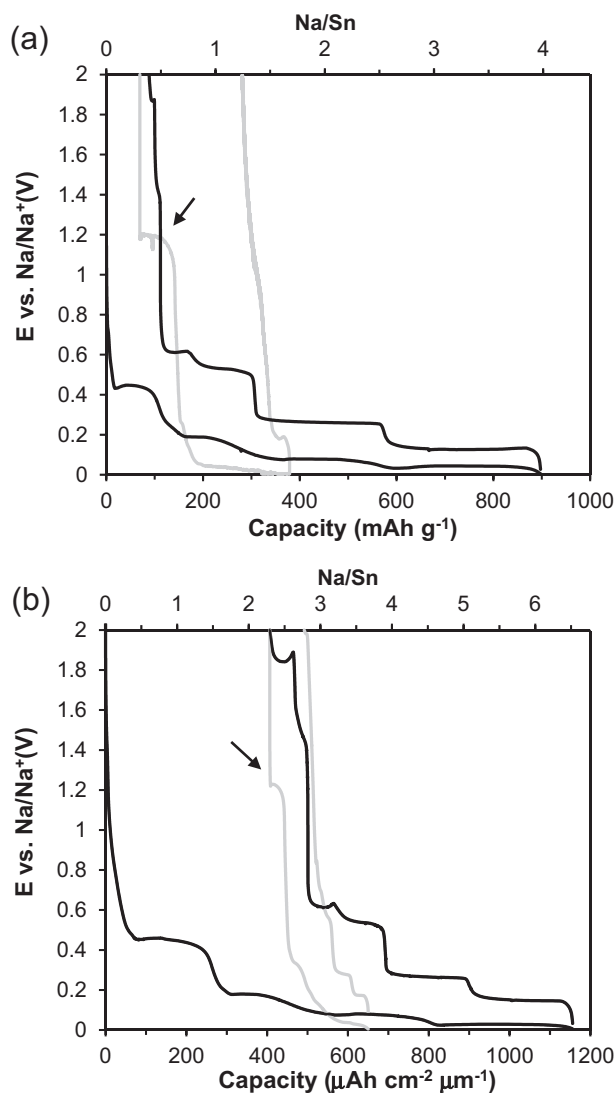


**Fig. 1.** Electrochemical potential profiles obtained during the first (black) and second (gray) cycles for (a) thick and (b) thin Sn film electrodes cycled between 0.005 and 2 V. Figure (a) shows the first cycles obtained on a micro-weighted 2 μm thick Sn electrode and a typical second cycle. The electrode was measured using 15.79 μA cm<sup>-2</sup> discharge current and 7.89 μA cm<sup>-2</sup> charge current, respectively C/70 and C/130. Figure (b) shows the first cycles' potential profiles for a 100 nm thick Sn electrode measured with a current of 3.95 μA cm<sup>-2</sup>. The arrow highlights the anomalous high voltage plateau measured during the second discharge.

### 3.1.1. Understanding plateaus in the electrochemical profile

As reported earlier, the potential profiles (Fig. 1) upon initial inspection consist of four plateaus, denoted from 1 to 4 in Fig. 2, which are attributed to bi-phasic reactions [8,9]. For Na/Sn contents larger than about 0.5–0.6 Na/Sn, three conjugated plateaus are observed during discharge and charge, as numbered 2, 3 and 4 in Fig. 2. All plateaus, except charge plateaus 2 and 3, systematically start with a potential dip (typically 10–20 mV, depending on the current) followed by an increase of potential. Ellis et al. speculated that these features are not thermodynamic but linked to an improvement of the Na-ion diffusion as (de)alloying progresses [9]. It is clear that the features are kinetic in nature, however, the increase and decrease in potential are more likely related to the nucleation and growth of the new phase clusters, as is generally observed on many bi-phasic electrode systems, such as Sn, Si or LiFePO<sub>4</sub> for Li-ion systems [18–20] and generally described for electrochemically induced phase transitions [21].

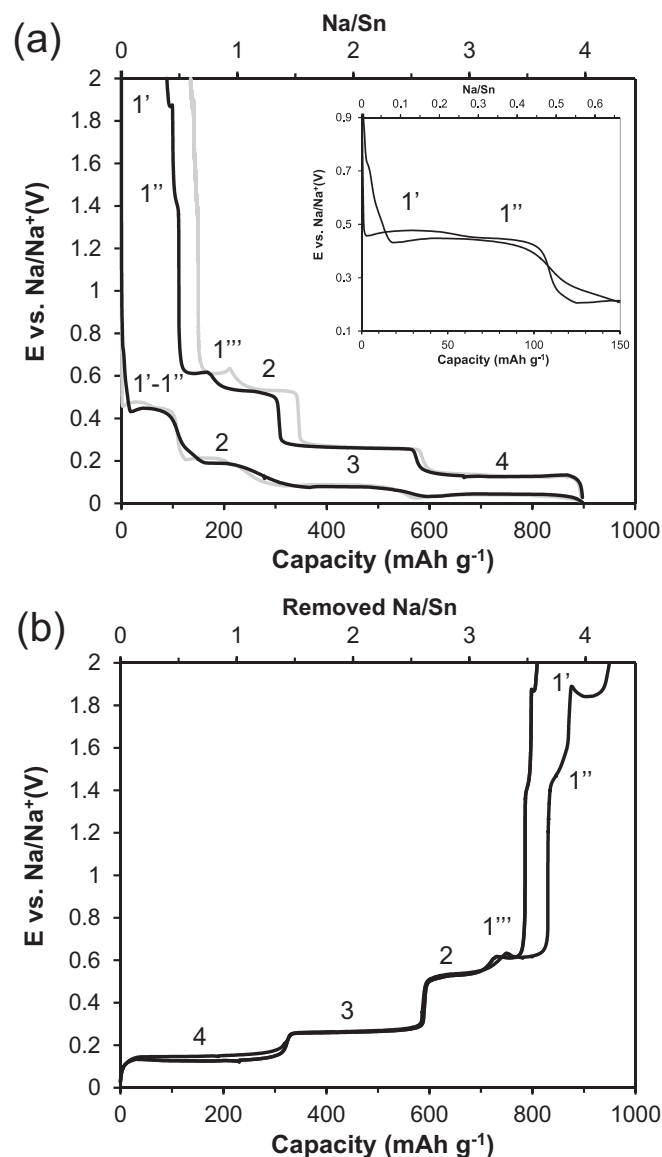


**Fig. 2.** (a) First two electrochemical cycles of a micro-weighted thick electrode (first cycle also presented in Fig. 1a) between 0.005 and 2 V. 17 h rest was allowed between the first (black curve) and second (gray curve) cycles. First cycle was measured at 15.79 μA cm<sup>-2</sup> (C/70) during discharge and 7.89 μA cm<sup>-2</sup> (C/130) during charge and second cycle was measured with 7.89 μA cm<sup>-2</sup> (C/130). The inset shows the start of the discharges, highlighting the presence of two plateaus when using a lower current, from 0 to 0.25 Na/Sn and from 0.25 to 0.5 Na/Sn. Figure (b) compares the first cycle charge potential profiles (amount of Na/Sn removed from the electrode) shown in Fig. 1a and b for a thick and thin electrodes. The numbers denote the different plateaus.

Several other reactions not yet described by others [8,9] are also present during Na-ion (de)insertion. For example the first plateau around 0.45 V during discharge (Fig. 1a) may actually be composed of two plateaus, as discerned on a thin electrode (Fig. 1b) and clearly visible on Fig. 2a when using a current below C/100 during the second cycle. This double plateau at 0.45 V was only obtained during the second discharge after full desodiation at 2 V during the first charge (Fig. 2a), and is also visible in the data presented in Ref. [9]. Given the similar voltages of these plateaus, we denote them 1' and 1''. These plateaus encompass Na/Sn contents ranging from 0 to 0.25 and from 0.25 to 0.5. The Na–Sn system includes several phases for low Na contents, i.e. NaSn<sub>5</sub>, NaSn<sub>4</sub>, Na<sub>5</sub>Sn<sub>13</sub>, NaSn<sub>2</sub>, Na<sub>7</sub>Sn<sub>12</sub> [22], some of which may be formed during the reactions associated with these plateaus.

Moreover, an inflexion around 0.25 V is present during the first discharge (Fig. 1a), as also visible in Ref. [9] and clearly revealed in our GITT data (see Fig. 4c).

In addition to the conjugated plateaus 2, 3 and 4, we have observed several additional features at low Na/Sn ratios, *i.e.* potentials higher than 1 V, with an inflexion near 1.4 V and a plateau near 1.9 V. Interestingly, these features are more pronounced on thin electrodes than on thick electrodes (Fig. 2b). These features have not been reported, and the impression has been given that the charge spent on the four plateaus is intimately correlated since the first desodiation and second sodiation were normalized (Fig. 3 in Ref. [9]). However, in Fig. 1 of Ref. [9] one can observe that plateau 1 during the first sodiation is wider than plateau 1 during the second sodiation. The difference in width lies in the remaining Na that is not totally extracted when using a cut-off potential of 0.8 V. As our results also indicate, there is a good correlation of capacity between plateaus 2, 3 and 4 during (dis)charge, however this is not the case for plateau 1 ( $1' + 1''$ ) at 0.45 V during discharge and the plateau  $1'''$  near 0.6 V during charge. A more accurate description of the reaction includes plateaus  $1'$ ,  $1''$  and  $1'''$ , as presented in Fig. 2.

The electrode reactions appear to be essentially independent of electrode thickness, with the exception of the high voltage plateaus during charge that are more pronounced for thin (100 nm) electrodes than thick (2  $\mu\text{m}$ ) electrodes (Fig. 1). We attribute this difference to either faster solid-state diffusion kinetics or improved mechanical integrity during full contraction associated with full desodiation of thin films. It could also be that partial oxidation of the electrode surface is facilitated on thin films due to cycling at lower current densities (see discussion on XPS data). When using thin electrodes (Fig. 1b) the irreversible capacity is a much larger fraction of the total capacity and is attributed to the electrolyte decomposition. This higher irreversible capacity can be explained by the much larger surface to volume ratio of thin electrodes and the smaller current densities used on thinner films. Moreover, it was determined that the application of even low current densities (0.39 or 0.79  $\mu\text{A cm}^{-2}$ ) induced the presence of an anomalous high voltage plateau at 1.2 V vs Na/Na<sup>+</sup> during the first discharge (data not presented here), which was also mentioned by Ellis et al. using a different electrolyte [9]. This plateau is also clearly visible at higher current densities during the second discharge for electrodes that were continuously cycled (Fig. 1). However, when the electrode is permitted a rest time of 17 h at the end of charge at 2 V, the following discharge appears normal (Fig. 2a). It is worthwhile mentioning that the plateau at 1.2 V accompanied with a poor cycleability is also measured when a rest of only 8 h is applied. In the case of the Li–Sn system, this anomalous plateau was attributed to the catalytic decomposition of the electrolyte onto the fresh Sn nanosized particles created during charging [18]. The XPS data presented later will indicate that surface oxides are in fact responsible for this decomposition.

### 3.1.2. Reversibility of electrode reactions

It was found that the charge and discharge cut-off voltages influence the electrochemical profiles of thin electrodes on cycling, indicating that the electrochemical reactions may take a different reaction pathway (Fig. 3). Charging the electrode only up to 0.4 or 0.6 V alters the subsequent discharge in the low potentials region (Fig. 3a). The discharge plateaus 3 and 4 that are normally observed at 0.07 and 0.03 V (*e.g.*, in Fig. 2) are present at sensibly higher potentials around 0.08 and 0.05 V, respectively. When charging up to 0.7 V (data not presented) the discharge profile is essentially the same as during the first discharge; the plateau at 0.45 V (plateau 1) during discharge is, however, less wide, as reported in Ref. [9]. This indicates that the starting material already contains Na and that the

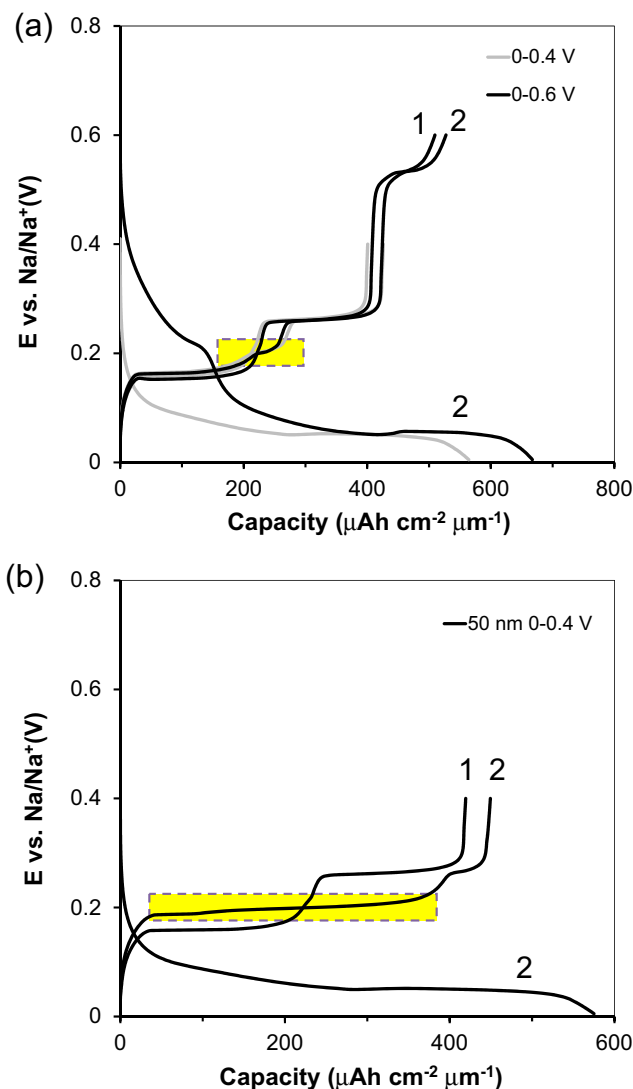


**Fig. 3.** (a) Electrochemical potential profiles measured on 100 nm thick electrodes cycled between 0–0.4 V and 0–0.6 V. (b) Potential profiles of a 50 nm thick Sn electrode during the first two cycles. For clarity, only the second discharge is presented, see Fig. 1b for a typical first discharge. The first charge and subsequent discharge and charge are shown as indicated by the numbers. The box encompasses a new plateau observed upon cycling, representing a new reaction pathway. A current of 3.95  $\mu\text{A cm}^{-2}$  was used.

reactions above 0.7 V during charging consist of Na-ion removal, as found for the Li–Sn system [10].

During discharge, restricting the voltage to 0.06 V suppresses the plateau around 0.12 V during charge (data not presented), confirming that the plateaus denoted 4, at 0.03 V during discharge and 0.15 V during charge, are conjugated. More interestingly, the plateaus at 0.15 V (plateau 4) and 0.26 V (plateau 3) during the initial charge are replaced by a single plateau at 0.2 V encompassing their summed capacities in subsequent cycles, as highlighted by the boxes in Fig. 3. The transition to a single plateau is partial in the 100 nm film and nearly complete in the 50 nm film. This change is indicative that upon cycling with a 0.4 V cut-off the reaction proceeds using a different reaction pathway; based upon capacity data, the reaction may proceed directly from  $\text{Na}_{15}\text{Sn}_4$  at 0 V to a material of composition near  $\text{Na}_{12}\text{Sn}$ . As the appearance of the new plateau was not evidenced on thick layers, it was not possible to elucidate this change by means of XRD using thin layers. The phase formed on plateau 3 during the initial discharge has the electrochemical

composition of  $\text{Na}_{2.4}\text{Sn}$ , nominally  $\text{Na}_5\text{Sn}_2$  (see later), and is shown here to be metastable. As such, it is perhaps unsurprising that the repeated reaction proceeds without its formation. Another plausible explanation is that the formation of  $\text{Na}_{15}\text{Sn}_4$  is avoided and the thermodynamically stable  $\text{Na}_{3.7}\text{Sn}$  ( $\text{Na}_{14.8}\text{Sn}_4$ ) [22] is formed instead. As a result, this phase may convert directly into the amorphous phase of composition close to  $\text{Na}_{1.2}\text{Sn}$ .

### 3.2. Computational and experimental results

The quasi-equilibrium potential profiles obtained by GITT are presented for a thin Sn electrode in Fig. S2 and for a thick electrode in Fig. 4. As found with constant current measurements, thinner electrodes have larger irreversible capacities. However, the Na–Sn reaction voltages are similar. Well defined plateaus are visible at potentials much closer to their true thermodynamic values. Comparison of the calculated potential values obtained from DFT calculations, which use a two-phase coexistence approximation using the ICSD phases, to the constant current and quasi-equilibrium potential profiles is shown in Fig. 4a and b, respectively. While the DFT calculations seem to agree fairly well with the average potentials from the constant current measurements, similar to what was seen from previous such calculations with a different set of ICSD phases [5,9], the DFT calculations somewhat underestimate the average GITT potential at large Na/Sn ratios. The difference in potential between galvanostatic and GITT measurements is related to the overpotentials, which are found to be of asymmetric distribution. From comparison between DFT and the GITT measurement, it appears that more overpotentials are relaxed during discharge (sodiation) in comparison with charge (desodiation); overpotentials result from either poorer kinetics of the surface charge transfer, slower diffusion of  $\text{Na}^+$  ions in the bulk, or a different reaction pathway for the charge

and discharge curves. As a result the discharge profile of the GITT measurement is shifted upwards more so than the charge profile. The use of  $\text{Na}_5\text{Sn}_2$  instead of  $\text{Na}_9\text{Sn}_4$  in the potential profile calculation has only a little impact on the predicted voltage, which changes from 0.140 to 0.133 V for the transition from Na–Sn, and therefore cannot explain why the calculated potentials would be lower than the measured reaction potentials.

Cluster-expansion based structure predictions [16] lead to several new phases that lie below the convex hull formed by data from ICSD, especially at  $\text{Na/Sn} \leq 2.5$  (Table S1). New phases are predicted at  $x = 2.5, 2, 0.6, 0.5, 0.33$  and  $0.143$ . Only the lowest energy phases for each symmetry of the Sn-host structure are shown for convenience in Fig. 4c and are also plotted as function of Na/Sn in Fig. 4d. It is interesting to note that many more new phases are predicted at lower Na contents, especially below  $\text{Na/Sn} = 2.5$ . There are also significantly more metastable phases (not shown) in all our studied Sn-host structures for  $\text{Na/Sn} \leq 2.5$ . This indicates high Na miscibility in Sn and also explains the reaction non-reversibility observed during discharge and charge. Some of the structures are layered and might perhaps be preferred due to a lower kinetic barrier expected in layered compounds. In addition, presence of different low-energy phases with different symmetries which are close in energy suggests an increased ease of forming amorphous structures due to frustration and sluggish kinetic effects. Moreover a predicted phase of composition  $\text{Na/Sn} = 2.5$  was identified in our experiments (see next). These predictions may explain the XRD data discussed below.

### 3.3. Structural characterization

*Ex situ* XRD was conducted with Cu  $K_\alpha$  and Mo  $K_\alpha$  radiations, Fig. S3 and Fig. 5 respectively. The data collected under both sources

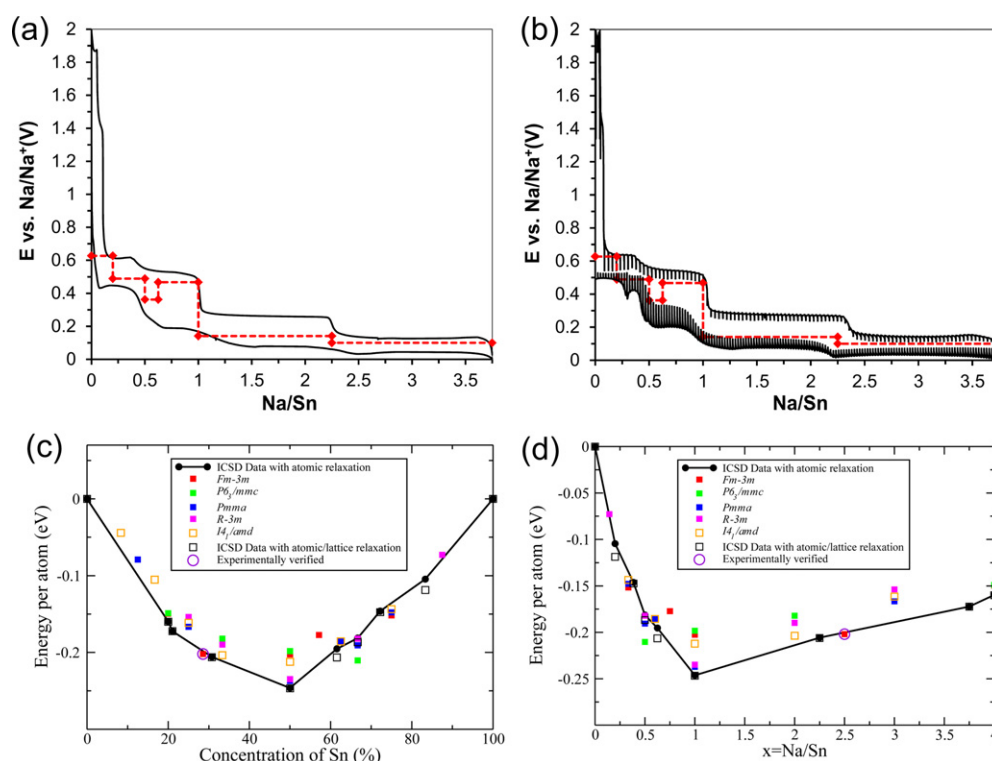


**Fig. 4.** Comparison of the potential profile obtained from galvanostatic (a) and GITT (b) measurements for 2  $\mu\text{m}$  thick Sn electrodes, including potential calculations obtained from DFT calculations. GITT discharge is obtained during the second cycle and GITT charge during the first cycle. Capacities are normalized to 3.75 Na/Sn. Formation energies per atom as a function of (c) Sn concentration and (d) Na/Sn ratio as described by Equations (1) and (2). Only the ground state structures from each Sn-host lattice investigated in our cluster-expansion study have been included in these plots.

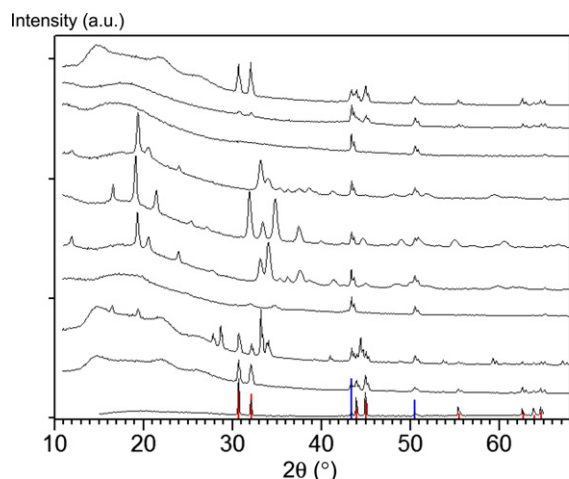


**Fig. 5.** X-ray diffraction patterns collected on Na–Sn electrodes during the first cycle, discharging from 0.5 to 0.005 V then charging up to 0.7 V. The patterns were obtained with Mo  $K_\alpha$  radiation but converted to Cu  $K_\alpha$  for ease of comparison. The pattern at 0.5 V obtained with Cu  $K_\alpha$  (see Fig. S3) is added for reference. The red and blue bars indicate  $\beta$ -Sn and Cu reference patterns, respectively. The broad humps at low angles result from Kapton. (For interpretation of the references to color in this figure legend, the reader is referred to the web version of this article.)

is similar except that Mo  $K_\alpha$  radiation, which is more intense and has a higher penetration through Kapton due to its smaller wavelength, yields higher quality of data for these experiments (Fig. 5). The structural parameters resulting from the XRD data are summarized in Table 1. The patterns obtained at 0.25 V, 0.12 V, 0.06 V and 0 V correspond to the end of sodiation of plateaus 1', 2, 3 and 4, and the patterns obtained during charge at 0.2, 0.4, 0.6, 0.7 V correspond to the end of desodiation from plateaus 4, 3, 2 and 1', respectively (Fig. 2). At full sodiation, the formation of  $\text{Na}_{15}\text{Sn}_4$  is clearly evidenced with a refined lattice parameter of 13.175 Å. The slightly larger lattice parameter compared to the reported 13.146 Å [9] can be related to a slight Na overstoichiometry, and corresponds to only about 0.2% increase in lattice parameter. The formation of this phase was evidenced for electrodes discharged below C/100 or for electrodes short-circuited overnight, which indicates that the reaction is completed in both cases. The formation of  $\text{Na}_{15}\text{Sn}_4$  phase corresponds to a volume expansion of about 430% or a final to initial volume ratio of about 5.3 compared to  $\beta$ -Sn.

At 0.06 V during discharge or 0.2 V during charge a new crystalline structure is measured (Fig. 6a). The peak positions for both structures are the same but the intensity ratios differ depending on whether the electrode is sodiated or desodiated (this difference was consistently found). The data presented by Ellis et al. seems to indicate the same results although the figure in which this data is presented is too small to unambiguously answer [9]. The difference in peak intensity may result from a difference in preferred orientation of the crystallites inside the film, from insufficient particle statistics, or from slight differences in crystal structure and composition. To better understand the role of different contributions to the diffraction pattern in these thin film samples, Rietveld refinements were carried out on data collected for the as deposited  $\beta$ -Sn film. The tetragonal  $\beta$ -Sn structure contains only a single crystallographic site, which is a fixed special position, and therefore any differences in the relative intensities must relate to factors other than atomic position. Differences were observed in the relative intensities that could only be treated by including a slight preferred orientation correction, and free refinement of the atomic displacement parameter ( $U_{\text{iso}}$ ) led to unphysical negative values. The use of a surface roughness absorption correction was not successful in producing positive  $U_{\text{iso}}$  parameters. The differences in fit

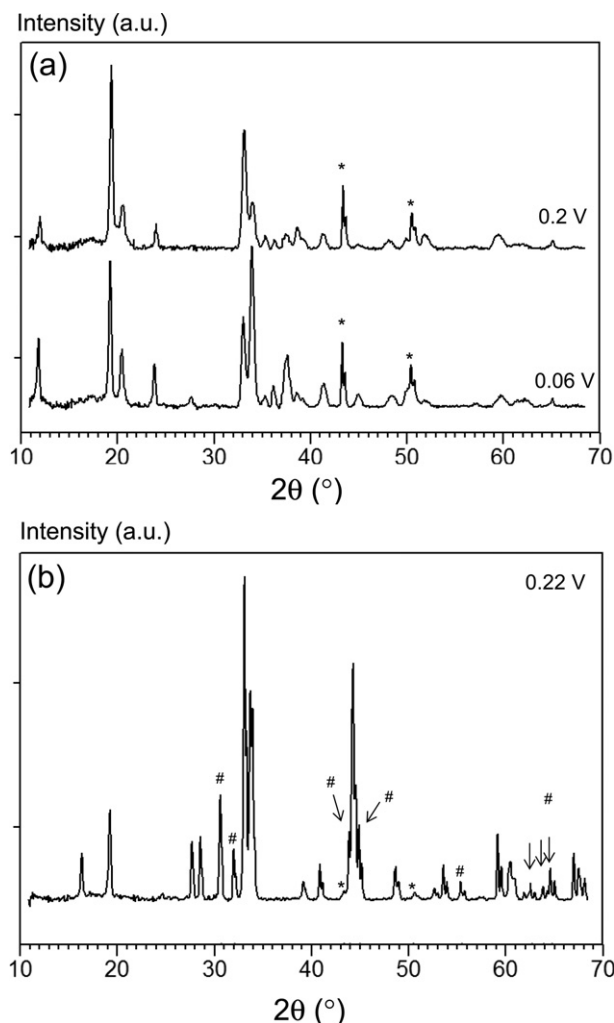


**Fig. 6.** (a) X-ray diffraction patterns collected on Na–Sn electrodes at 0.06 V during discharge and 0.2 V during charge, corresponding to the  $R\bar{3}m$  phase of nominal composition  $\text{Na}_5\text{Sn}_2$  and electrochemical composition of  $\text{Na}_{2.4}\text{Sn}$ . (b) X-ray diffraction patterns collected on Na–Sn electrodes at 0.22 V during discharge, corresponding to an unidentified phase of electrochemical composition around  $\text{Na}_{0.6}\text{Sn}$ . (\*) and (#) correspond to Cu and  $\beta$ -Sn, respectively. Beam overflow is corrected at low angles and backgrounds are subtracted.

are likely related to preferred orientation, though insufficient particle statistics may play a role. An optimum fit for Sn is given in Fig. S5, including the spherical harmonic preferred orientation correction. The  $\text{Na}_{15}\text{Sn}_4$  phase formed at 0 V is expected to be polycrystalline and fairly randomly oriented, given that the formation of a preferentially oriented structure from the amorphous/nanocrystalline phase formed at 0.12 V is unlikely. Furthermore, the  $\text{Na}_{15}\text{Sn}_4$  structure is cubic ( $I\bar{4}3d$ ), and therefore potentially less susceptible to preferred orientation effects. Nonetheless, we cannot completely rule out this possibility given the Rietveld refinement results for Sn. Refined X-ray diffraction data for  $\text{Na}_{15}\text{Sn}_4$  are shown in Fig. S6, and indeed include a preferred orientation correction.

The diffraction positions for both 0.06 V discharged and 0.2 V charged electrodes match very well those of  $\text{Li}_5\text{Sn}_2$  after adjusting the original lattice parameters ( $a = b = 4.74$  Å and  $c = 19.83$  Å) of the hexagonal  $R\bar{3}m$  structure. Refining the patterns yields lattice parameters of  $a = b = 5.397$  Å and  $c = 22.257$  Å for the 0.06 V discharged electrode, and  $a = b = 5.416$  Å and  $c = 22.377$  Å for the 0.2 V charged electrode (Table 1). A list of ( $hkl$ ) reflections is given in Table S2 and the list of refined  $z$  positions is given in Table 2. Given

**Table 2**

Atomic positions obtained after refinement of the XRD patterns measured at 0.06 V during discharge and 0.2 V during charge, using a  $R\text{-}3m$  unit cell derived from  $\text{Li}_5\text{Sn}_2$ . Due to the strong attenuation of the (003) peak by Kapton, only the  $z$  positions were refined.

Material	Atoms	Occupancy	$x$	$y$	$z$
$\text{Li}_5\text{Sn}_2$	Li1 3b	1	0	0	0
	Li2 6c	1	0	0	0.1480
	Li3 6c	1	0	0	0.2900
	Sn 6c	1	0	0	0.4273
Discharge 0.06 V	Na1 3b	1	0	0	0
	Na2 6c	1	0	0	0.1505
	Na3 6c	1	0	0	0.2978
	Sn 6c	1	0	0	0.4377
Charge 0.2 V	Na1 3b	1	0	0	0
	Na2 6c	1	0	0	0.1502
	Na3 6c	1	0	0	0.3433
	Sn 6c	1	0	0	0.4344

the strong attenuation at low angles by the Kapton tape, especially for the (003) peak, atomic occupancies were not refined. It was possible to achieve a stable refinement including the positions, and in general a fairly good match is found for the  $z$  positions between the refined patterns and the starting  $\text{Li}_5\text{Sn}_2$  structure. Moreover, the structural parameters of this phase are in good agreement with the predictions from the cluster-expansion method and the predicted lattice parameters differ by only about 1.5% from experiments. It is worthwhile mentioning that preferred orientation corrections are required in this case, as was found for  $\beta\text{-Sn}$  and  $\text{Na}_{15}\text{Sn}_4$ . A number of lower symmetry subgroups of  $R\text{-}3m$  were explored, including  $C2/m$  and  $R3m$ . The  $R\text{-}3m$  structure has 3 crystallographically distinct Na sites (6c and 3b) and one Sn site (6c), with a cell volume of  $\sim 566.9 \text{ \AA}^3$ . The  $R3m$  subgroup has the same cell volume, but with 2 additional Na sites. The  $C2/m$  subgroup has a smaller cell volume ( $\sim 375 \text{ \AA}^3$ ) and the same number of sites, but two of the Na sites (4i) have additional freedom along the  $a$  axis. A refinement in the  $C2/m$  monoclinic structure ( $a = 9.374 \text{ \AA}$ ,  $b = 5.380 \text{ \AA}$ ,  $c = 8.024 \text{ \AA}$  and  $\beta = 112.39^\circ$ ) is shown in Fig. S7. Refinement in the lower symmetry structures has the effect of improving the fit quality. However, the improved fit requires either a significantly larger preferred orientation correction ( $R3m$ ) or  $U_{\text{iso}}$  ( $C2/m$ ), and it is therefore difficult to ascertain whether the decrease in symmetry is warranted. Therefore, we will tentatively assign the  $R\text{-}3m$  structure for  $\text{Na}_5\text{Sn}_2$ , and refinement results are presented in Fig. S8 (discharge) and Fig. S9 (charge).

The other crystalline phase forming during discharge is visible at 0.25 V (Fig. 5), or at 0.22 V (Fig. 6b). Our pattern has several additional peaks compared to the pattern reported previously (compare the double peak at about  $2\theta = 34^\circ$  in Ref. [9]) and generally a much higher intensity. This results from the use of a thick ( $5 \mu\text{m}$ ) Sn starting film, penetrating Mo  $K_\alpha$  radiation and a smaller step size. This phase does not have any conjugate phase during charge as the material formed at 0.6 V during charge consists of an amorphous phase along with a small fraction of  $\beta\text{-Sn}$ . The phase formed here during discharge also clearly comprises a small fraction  $\beta\text{-Sn}$ , which is also visible in the corresponding XRD pattern of plateau 1 in Ref. [9]. Fifteen independent reflections were observed, in addition to those of Sn and Cu (Fig. S10). A number of viable unit cells were identified, but there was insufficient information from the available XRD data to determine a model of the crystal structure. Measurements on electrodes at 0.34 V (not presented here) indicate the same diffraction lines, which indicate that the phase is formed at the end of plateau 1. The potential of 0.22 V was selected to be as close as possible to the start of plateau 2, the persistence of  $\beta\text{-Sn}$  is nonetheless clearly measured. This persistence thus far in the discharge is probably related to the slow diffusion kinetics of Na

ions in thick electrodes leading to a gradient of Na concentration throughout the film. It could also be that the small plateau near 0.25 V visible during the second discharge (Fig. 4b) is related to the full consumption of  $\beta\text{-Sn}$ . The structure of this unknown crystalline phase of composition determined at about  $\text{Na}_{0.6}\text{Sn}$  is yet to be resolved.

Using TEM in combination with SAED, we have further characterized various electrodes discharged at 0.06 V or charged at 0.2 V (Fig. 7a). The harvested electrode materials consist of nanoparticle clusters, which yield ring patterns when SAED is acquired. The experimentally measured lattice spacings (Table S3) match several of those expected for  $\text{Na}_5\text{Sn}_2$  (Table S2), confirming the  $R\text{-}3m$  space group assignment proposed from the diffraction data (Fig. 7b).

The XRD patterns measured for the discharged electrode at 0.12 V and the charged electrode at 0.4 V are somewhat similar (Fig. 8). The material formed during discharge is a mixture of amorphous and nanocrystalline phases whereas the material formed during charge at 0.4 V is amorphous. Given that total charge spent on the plateau 2 during discharge and charge are very similar, we suspect that the final compositions of these two phases is the same, their short range order structure is similar but that the ordering at longer range is facilitated during sodiation and is absent during desodiation. Efforts were also devoted to characterize the double plateau measured around 0.45 V during the second

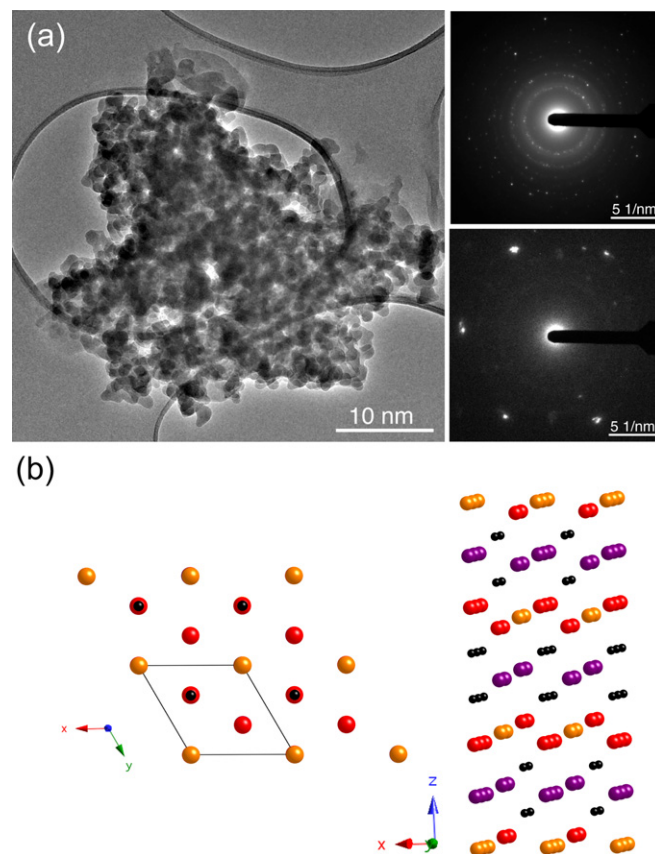


**Fig. 7.** (a) Representative bright-field TEM micrograph of the nanocrystalline Sn electrode material discharged to 0.06 V. Selected area electron diffraction ring patterns collected on Sn electrodes discharged to 0.06 V. (b) Postulated  $R\text{-}3m$  hexagonal structure for the new phase of nominal composition  $\text{Na}_5\text{Sn}_2$  and electrochemically determined at  $\text{Na}_{2.4}\text{Sn}$ . The structures schematics comprise 4 unit cells. Orange, red and purple atoms are distinctive Na sites and black atoms represent Sn. (For interpretation of the references to color in this figure legend, the reader is referred to the web version of this article.)

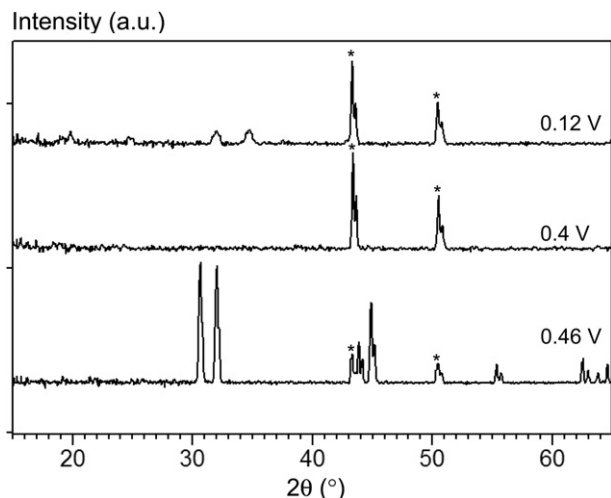


**Fig. 8.** X-ray diffraction patterns collected on Na–Sn electrodes at 0.46 V during discharge, 0.12 V during discharge and 0.4 V during charge. (\*) corresponds to Cu. In the pattern at 0.46 V all peaks except (\*) are resulting from  $\beta$ -Sn. Backgrounds are subtracted.

discharge (Fig. 2a). The XRD pattern collected after completion of plateau 1'' (Fig. 2a) is presented in Fig. 8 (0.46 V). Apart from Cu, the pattern shows reflections of only  $\beta$ -Sn. Given that the Na/Sn ratio at this point in the discharge is about 0.25, we suspect that Na is stored inside an amorphous phase growing at the expense of Sn.

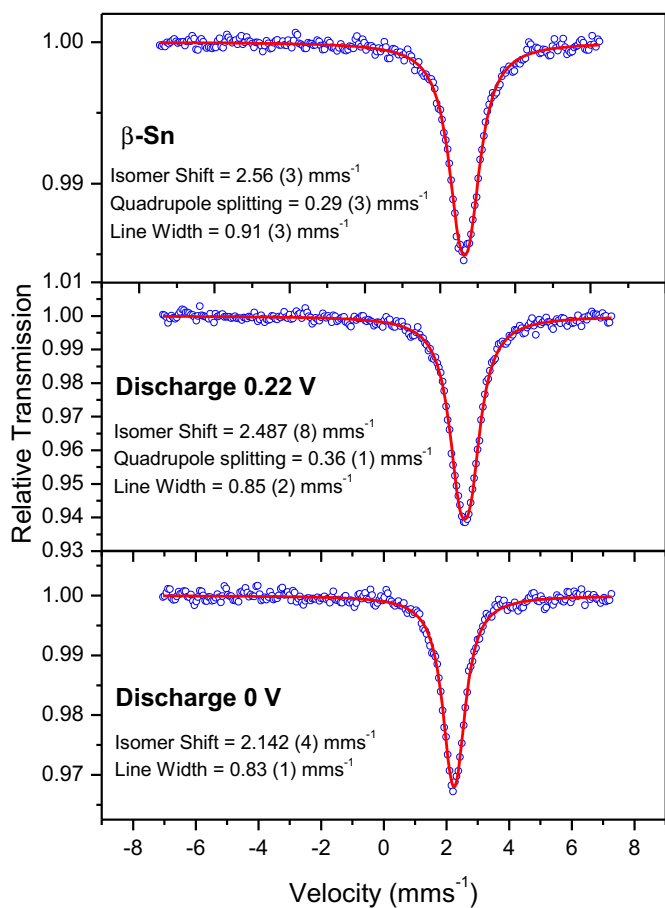


**Fig. 9.**  $^{119}\text{Sn}$  Mössbauer spectra for the electrodes discharged at 0.22 and 0 V, corresponding to the unknown crystalline phase formed at the end of plateau 1, and to  $\text{Na}_{15}\text{Sn}_4$ . The spectrum for  $\beta$ -Sn is included as reference.

The end of plateau 1' is characterized by the formation of an unknown crystalline phase (Fig. 6b) along with a small fraction of  $\beta$ -Sn. It is therefore likely that the consumption of Sn proceeds in three steps on the plateaus 1' and 1'' and on the small plateau at 0.25 V.

Mössbauer spectroscopy was measured during the first discharge to characterize the atomic environment of Sn atoms as a function of Na/Sn content. The initial measurements performed on 2  $\mu\text{m}$  thick films yielded very little absorption which made very difficult to resolve the spectra unambiguously. The low absorption observed on these electrodes resulted from the presence of  $\beta$ -Sn or sodiated Sn phases which have low expected recoil-free fractions for Mössbauer spectroscopy, as suggested by their relatively low melting points [22]. To obtain enough absorption two identical 6  $\mu\text{m}$  thick Sn film electrodes of larger surface area were measured together. The corresponding spectra for electrodes discharged at 0.22 and 0 V together with a reference for  $\beta$ -Sn (isomer shift of 2.560 (3)  $\text{mm s}^{-1}$ ) are presented in Fig. 9.

The spectrum at 0.22 V shows an unresolved doublet at 2.487 (8)  $\text{mm s}^{-1}$  with a weak quadrupole splitting (0.36 (1)  $\text{mm s}^{-1}$ ). By comparison with  $\beta$ -Sn the slight decrease of the isomer shift and the existence of a weak quadrupole splitting is in agreement with

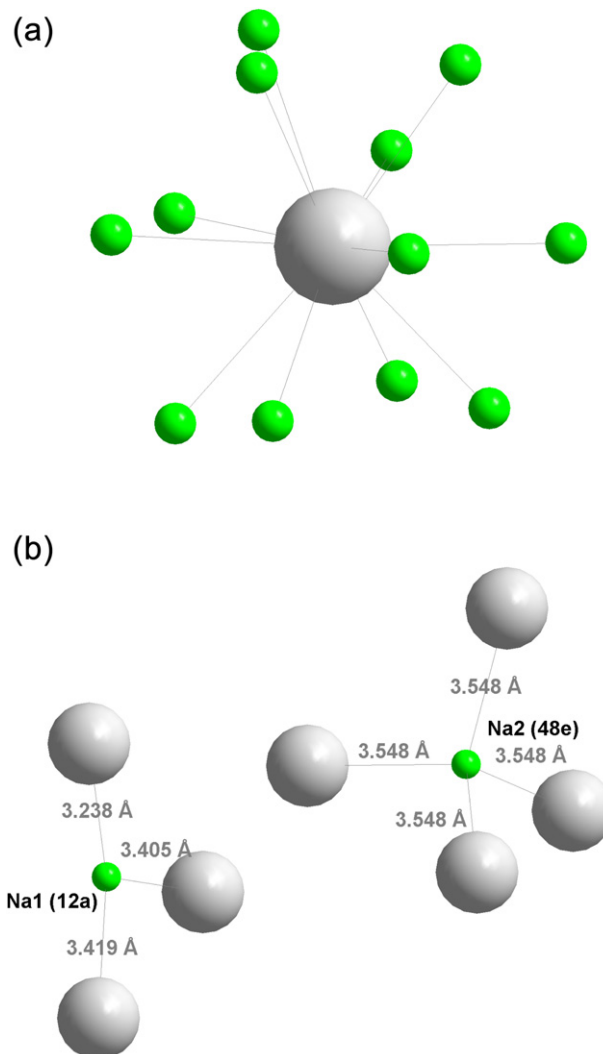


**Fig. 10.** Local coordination of  $\text{Na}_{15}\text{Sn}_4$  (I-43d). (a) Sn is 12 fold coordinated to Na. (b) planar 3-fold coordinated Na1 and tetrahedrally coordinated Na2.

a  $\text{Na}_x\text{Sn}$  alloy rich in Sn. At full sodiation the spectrum is composed of a singlet at  $2.142(4) \text{ mm s}^{-1}$ , which corresponds to a symmetric charge distribution over the Sn nucleus. This result is in good agreement with the structure of  $\text{Na}_{15}\text{Sn}_4$  (*I-43d*) that is made of isolated Sn atoms surrounded by Na atoms in relatively symmetric 12-fold coordination, with nearest neighbor Sn–Sn distances of  $\sim 5.6\text{--}5.9 \text{ \AA}$  and Sn–Na distances of  $\sim 3.2\text{--}3.5 \text{ \AA}$  (Fig. 10). The decrease in isomer shift as a function of increasing

Na/Sn content is analogous to what is found for the Li–Sn system [23]. For  $\text{Li}_7\text{Sn}_2$  ( $\text{Li}_{3.5}\text{Sn}$ ) and  $\text{Li}_{21+5/16}\text{Sn}_5$  ( $\text{Li}_{4.26}\text{Sn}$ ), the average isomer shifts are equal to 1.9 and  $1.83 \text{ mm s}^{-1}$ , respectively [23], whereas the isomer shift measured for  $\text{Na}_{15}\text{Sn}_4$  ( $\text{Na}_{3.75}\text{Sn}$ ) is near  $2.14 \text{ mm s}^{-1}$ . Similarly, the isomer shift for  $\text{Na}_{0.6}\text{Sn}$  (electrode at 0.22 V) at about  $2.49 \text{ mm s}^{-1}$  is higher than the interpolated isomer shift ( $2.40 \text{ mm s}^{-1}$ ) of a hypothetical  $\text{Li}_{0.6}\text{Sn}$  phase present in between  $\text{Li}_2\text{Sn}_5$  and  $\text{LiSn}$  [23]. The higher isomer shifts for

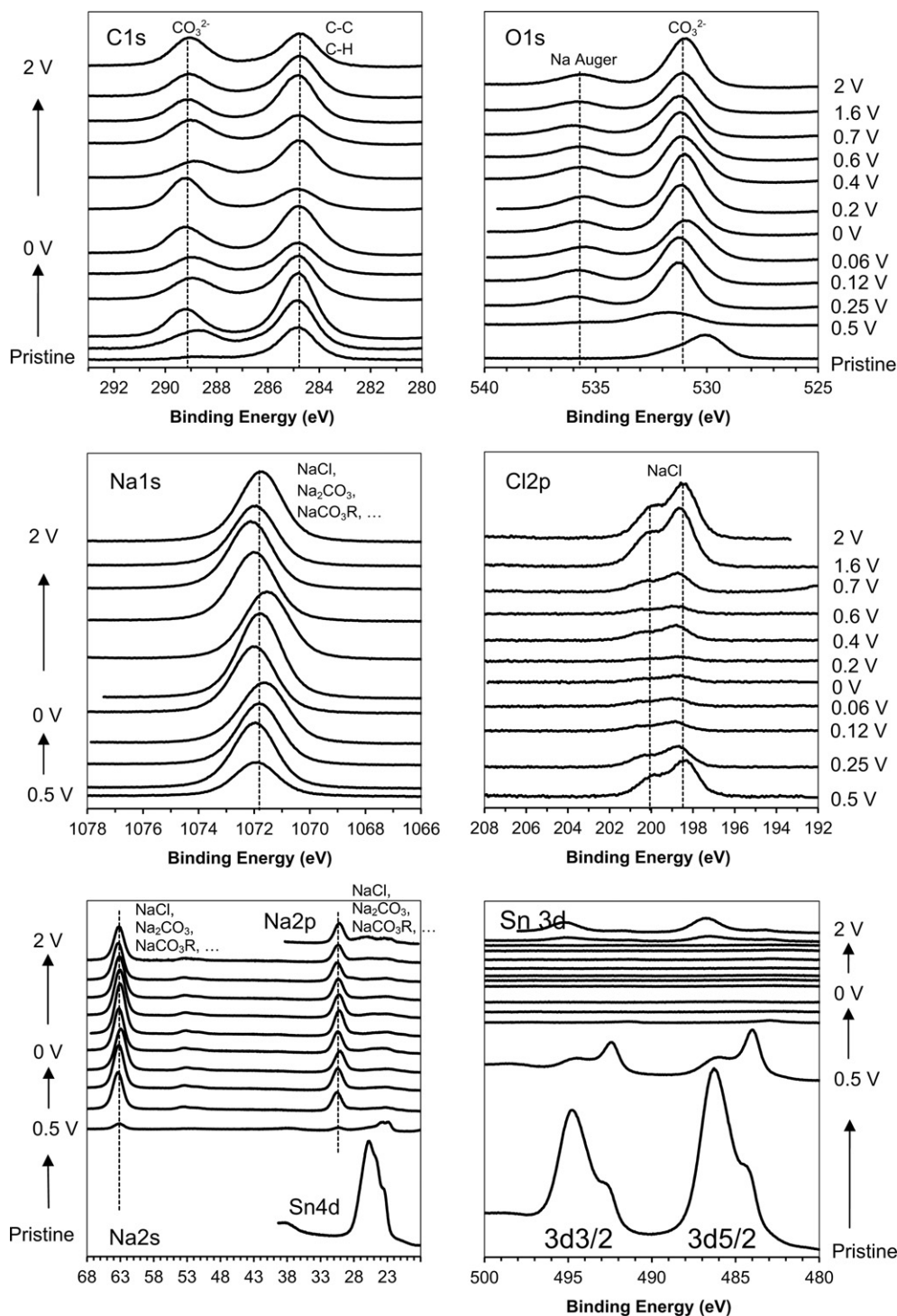


**Fig. 11.** X-ray photoelectron spectra collected on Sn electrodes during the first cycle, discharging from 0.5 to 0 V then charging up to 2 V (bottom to top).  $\text{Sn}3d$  spectra were collected with  $\text{Mg K}_\alpha$  radiation to avoid an important overlap with Na Auger lines. The other spectra were measured with  $\text{Al K}_\alpha$  radiation.

$\text{Na}_x\text{Sn}$  compared to  $\text{Li}_x\text{Sn}$  compounds can be related to the lower electropositivity of Na compared to Li, which results in a higher electron density on the Sn5s orbital of which the isomer shift is strongly dependent [23,24]. Efforts are currently devoted to measuring the other compositions of the potential profile curves to confirm the present trend in isomer shift.

### 3.4. Surface characterization

XPS was conducted in order to understand how the surface chemistry evolves with state of charge. The surface of the Sn pristine films is composed of an oxide bilayer made of  $\text{SnO}/\text{SnO}_2$ , as evidenced by the 3d and the 4d XPS core levels (Fig. S4). This result is in agreement with former works which clearly evidenced that  $\text{SnO}$  is covered by a thin layer of  $\text{SnO}_2$  [25]. In the case of  $\text{SnO}_2$  films, the surface is clearly only occupied by fully oxidized  $\text{Sn}^{4+}$  cations (Fig. S4) in a structure very close to, according to XRD, that of bulk stoichiometric  $\text{SnO}_2$  (Fig. S1). The surface of the electrode studied during the first cycle is presented in Fig. 11. The surface oxides are importantly reduced as pure Sn at 0.5 V, as supported by both Sn3d and 4d core levels – note that the O2s normally found around 23 eV is negligible for all measurements. Upon further sodiation, Sn signals become extremely weak. The Na signals (Na1s, Na2s and Na2p) remain more or less the same around 1072 eV in Na1s, 63.5 eV in Na2s and 29.5 eV in Na2p. Note that the peak around 53.5 eV is due to a Na loss peak. Measurements on  $\text{Na}_2\text{CO}_3$  dried powder yield a C1s main peak attributed to  $\text{CO}_3^{2-}$  at 289.2 eV, O1s at 530.8 eV, Na1s at 1071.2 eV, Na2s at 63.0 eV, a Na loss peak at 52.8 eV and Na2p at 30.3 eV. These values are in good agreement with the C1s, O1s and Na binding energies found here. In addition to  $\text{Na}_2\text{CO}_3$ , Na alkyl carbonates may be present with similar binding energies.

Upon close inspection of the Cl2p spectrum, there is evidence of NaCl on the surface. NaCl comes from the electrochemical reduction of  $\text{NaClO}_4$  but is also formed during the XPS measurement due to X-ray exposure. Survey scans measured for few minutes prior to any long high resolution scans indicated the presence of both  $\text{NaClO}_4$  and NaCl on the surface whereas prolonged exposure to X-rays, as shown in Fig. 11, clearly shows that all  $\text{NaClO}_4$  was reduced into NaCl after prolonged X-ray exposure. The same effect was observed on pure  $\text{NaClO}_4$  powder. To obtain a reference, we therefore measured three identical  $\text{NaClO}_4$  powders each measurement starting with a different core level of interest, i.e. Cl2p, O1s and Na1s. This way we obtained reliable data showing Cl2p3/2 peak at 207.0 eV and 2p1/2 peak at 208.7 eV, O1s at 532.9 eV and Na1s at 1072.2 eV. Essentially, the presence of NaCl found here is a large overestimate as most of Cl is initially present as  $\text{NaClO}_4$ . Carefully looking for such an effect on Sn core levels, no substantial changes in Sn binding energies were noticed after X-ray exposure. Anyway, in all cases the Sn signals were measured first to prevent possible changes during X-ray exposure.

Regarding the changes in oxidation state of Sn, we have identified the reduction of surface oxides into metallic Sn at 0.5 V followed by the formation of further reduced Sn species at 0.25 V, as characterized by a Sn 3d5/2 binding energy of about 483 eV (Fig. 11). This energy may be indicative of the formation of  $\text{Na}_x\text{Sn}$  compounds in which the 3s electron from Na is partly localized onto Sn. During the further discharge to 0 V and charge up to 0.7 V, the Sn signal has vanished due to the coverage of the electrode by the SEI material. To clarify discussion of the changes in oxidation state of Sn during charge at high potentials, the Sn 3d and 4d core levels spectra are plotted in Fig. 12. At 1.6 or 2 V, Sn 3d5/2 signals characteristics of reduced Sn species (483 eV) and oxidized  $\text{Sn}^{4+}$  species (486.5 eV) are observed. The observation of Sn signals indicates that the electrode surface gets exposed at the end of full charge. Exposure of Sn on the surface can be caused by the partial

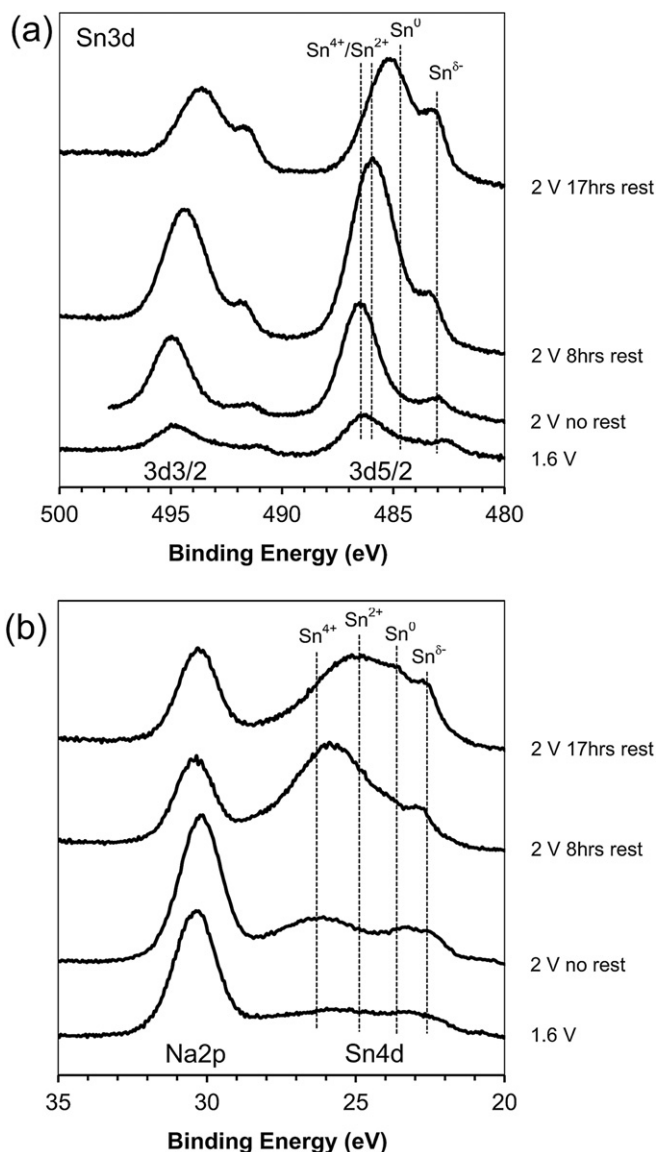


**Fig. 12.** X-ray photoelectron spectra Sn 3d and 4d collected on Sn electrodes when charged at 1.6 V, charged at 2 V without rest, 2 V with 8 h rest and 2 V with 17 h rest. 3d spectra were collected with Mg  $K_{\alpha}$  radiation to avoid overlap with Na Auger lines, 4d spectra were collected with Al  $K_{\alpha}$  radiation. Assignments on the 4d spectra are based on the binding energy of Sn oxides, as performed on the pristine materials (Fig. S2) and in Ref. [25].

removal of the SEI layer either electrochemically by oxidation or mechanically during the shrinkage of the electrode associated with desodiation.

The anomalous plateau at 1.2 V during the second discharge was previously attributed to the decomposition of the electrolyte on freshly made Sn nanoparticles for the Li–Sn system [18], an idea which was also retained in the recent work on Na–Sn [9]. We observe that pristine electrodes also provoke the electrolyte decomposition at very low currents. From this, we infer that pure Sn is not likely responsible for the electrolyte decomposition, as the Sn electrodes are always covered by a thin oxide layer when exposed to air (Fig. S4). We also observed that aging in the electrolyte after charging at 2 V leads to the complete absence of the plateau at 1.2 V accompanied with a drastic improvement in the cycleability during the second cycle (Fig. 2a). For these reasons we have studied the effect of electrolyte aging for cells charged at 2 V in

order to determine the subtle influences of surface oxides on the electrolyte decomposition.

When Sn electrodes charged at 2 V are aged in the electrolyte for 8 or 17 h (Fig. 12), important changes are observed on both core levels corresponding to a substantial decrease of the binding energies as a function of resting time, which is indicative of the reduction of Sn on the surface. The 4d core levels are more easily assigned, as found on the pristine material (Fig. S4) and by others on Sn oxides [25]. Assuming typical binding energies corresponding to Sn oxides, we have evidence that the electrode surface without aging is covered by  $\text{Sn}^{4+}$  species (4d binding energy of about 26.5 eV) and what is likely some reduced Sn in the form of  $\text{Na}_3\text{Sn}$  ( $\sim 22.5$  eV). Upon aging in the electrolyte, the binding energy decreases to about 25 eV and 23.5 eV, corresponding to  $\text{Sn}^{2+}$  and  $\text{Sn}^0$  species, respectively. When a long rest (17 h) is applied, the improvement in cyclability of the electrode (Fig. 2a) is attributed to the formation of reduced  $\text{Sn}^0$  and  $\text{Sn}^{2+}$  species on the surface. However, when no rest or a rest of 8 h are applied, a poor cycleability is measured (Fig. 1) and is attributed to the presence of oxidized  $\text{Sn}^{4+}$  species on the surface of Sn nanosized particles that are more prone to decomposing the electrolyte.

#### 4. Conclusions

We have thoroughly identified the Na-ion reaction mechanism of Sn using model thin films, coupled with detailed electrochemical, XRD and XPS characterizations. While the potential profile apparently involves a simple series of 4 plateaus on initial inspection, a more detailed analysis suggests that the mechanism is fairly complex. For example, an additional plateau at the start of discharge has been identified by employing very low currents. The plateau around 0.45 V is actually composed of two plateaus that collectively correspond to the transition from  $\beta$ -Sn to an amorphous phase. The subsequent plateau at 0.22 V during discharge relates to the formation of an unknown crystalline phase containing a minor amount of  $\beta$ -Sn. Furthermore, at least two more plateaus are present during charge above 0.7 V, not reported by Komaba et al. [8] or Ellis et al. [9], and correspond to the full desodiation of  $\text{Na}_3\text{Sn}$ . Moreover, upon cycling thin layers we have evidenced the suppression of the plateau related to the formation of the metastable  $R\text{-}3m$  phase of composition close to  $\text{Na}_5\text{Sn}_2$ . Instead a single plateau is present and may correspond to the direct transition from  $\text{Na}_{3.7}\text{Sn}$  or  $\text{Na}_{15}\text{Sn}_4$  into the nanocrystalline/amorphous phase of composition close to  $\text{Na}_{1.2}\text{Sn}$ .

$^{119}\text{Sn}$  Mössbauer spectroscopy was employed during the first charge to determine the atomic environment of the electrode material as a function of Na/Sn content. For example, the spectrum at full sodiation is consistent with a relatively symmetric 12-fold coordination environment of Na around Sn in  $\text{Na}_{15}\text{Sn}_4$ . Additionally, a decrease of the isomer shift is evidenced with increasing Na/Sn content. This decrease is less pronounced than for Li–Sn compounds, which is likely related to the lower electropositivity of Na compared to Li.

Our computational structure predictions using cluster-expansion methods have proved fruitful in identifying new thermodynamic ground-state phases, as well as metastable phases. While a phase at composition Na/Sn = 2.5 was identified in our experiments, the presence of other phases is not yet experimentally confirmed. The current study does not include effects of vibrational entropy, which is expected to alter the phase-diagram significantly at finite temperatures. Nevertheless, our experimental and computational results warrant a more detailed investigation of Na-ion

reaction kinetics and its effect on the thermodynamic voltage profile at different temperatures.

Finally, we have discovered that aging a fully charged electrode (2 V) in the electrolyte for 17 h completely suppresses the anomalous high voltage plateau at 1.2 V versus Na/Na<sup>+</sup>. Our XPS data indicate that  $\text{Sn}^{4+}$  species formed on the surface during charging are reduced when aging the electrode in the electrolyte. In turn, the reduced  $\text{Sn}^{2+}$  and  $\text{Sn}^0$  species do not appear to be active for decomposing the electrolyte. The anomalous high voltage plateau occurs when  $\text{Sn}^{4+}$  present on the surface of Sn nanoparticles promotes the irreversible decomposition of the electrolyte, detrimentally affecting the electrode capacity retention.

#### Acknowledgments

This work was supported by the U.S. Department of Energy (DOE), Basic Energy Sciences (BES), Materials Sciences and Engineering Division. Research supported by ORNL's Shared Research Equipment (ShaRE) User Program (Microscopy) and computations performed at the Center for Nanophase Materials Sciences (CNMS) are both sponsored by DOE-BES. JCJ gratefully acknowledges Region Languedoc-Roussillon (France) for the financial support to the "X-rays and gamma-rays platform" of Université Montpellier II in relation with Mössbauer spectroscopy experiments.

#### Appendix A. Supplementary data

Supplementary data related to this article can be found at <http://dx.doi.org/10.1016/j.jpowsour.2013.01.083>.

#### References

- [1] S.-W. Kim, D.-H. Seo, X. Ma, G. Ma, K. Kang, *Adv. Energy Mater.* 2 (2012) 710–721.
- [2] B.L. Ellis, L.F. Nazar, *Curr. Opin. Solid State Mater. Sci.* 16 (2012) 168–177.
- [3] N. Yabuuchi, M. Kajiyama, J. Iwatate, H. Nishikawa, S. Hitomi, R. Okuyama, R. Yasuhiro, S. Komaba, *Nat. Mater.* 11 (2012) 512–517.
- [4] P. Senguttuvan, G. Rousse, V. Seznec, J.-M. Tarascon, M.R. Palacin, *Chem. Mater.* 23 (2011) 4109–4111.
- [5] V.L. Chevrier, G. Ceder, *J. Electrochem. Soc.* 158 (2011) A1011–A1014.
- [6] L. Xiao, Y. Cao, J. Xiao, L. Kovarik, Z. Nie, J. Liu, *Chem. Commun.* 48 (2012) 3321–3323.
- [7] Y. Xu, Y. Zhu, Y. Liu, C. Wang, *Adv. Energy Mater.* (2012). <http://dx.doi.org/10.1002/aenm.201200346>.
- [8] S. Komaba, Y. Matsuura, T. Ishikawa, N. Yabuuchi, W. Murata, S. Kuze, *Electrochem. Commun.* 21 (2012) 65–68.
- [9] L.D. Ellis, T.D. Hatchard, M.N. Obrovac, *J. Electrochem. Soc.* 159 (2012) A1801–A1805.
- [10] H. Krüger, R.X. Fischer, *J. Appl. Crystallogr.* 37 (2004) 472–476.
- [11] G. Kresse, J. Furthmüller, *Phys. Rev. B* 54 (1996) 11169–11186.
- [12] G. Kresse, D. Joubert, *Phys. Rev. B* 59 (1999) 1758–1775.
- [13] P.E. Blochl, *Phys. Rev. B* 50 (1994) 17953–17979.
- [14] I.A. Courtney, J.S. Tse, O. Mao, J. Hafner, J.R. Dahn, *Phys. Rev. B* 58 (1998) 15583–15588.
- [15] D. de Fontaine, *Solid State Phys.* 47 (1994) 33–176.
- [16] A. van de Walle, G. Ceder, *J. Phase Equil.* 23 (2002) 348–359.
- [17] A. van de Walle, M. Asta, G. Ceder, *Calphad* 26 (2002) 539–553.
- [18] S.D. Beattie, T. Hatchard, A. Bonakdarpour, K.C. Hewitt, J.R. Dahn, *J. Electrochem. Soc.* 150 (2003) A701–A705.
- [19] L. Baggetto, R.A.H. Niessen, F. Roozeboom, P.H.L. Notten, *Adv. Funct. Mater.* 18 (2008) 1057–1066.
- [20] G. Oyama, Y. Yamada, R.-I. Natsui, S.-I. Nishimura, A. Yamada, *J. Phys. Chem. C* 116 (2012) 7306–7311.
- [21] M.D. Levi, D. Aurbach, *J. Solid State Electrochem.* 12 (2008) 409–420.
- [22] J. Sangster, C.W. Bale, *J. Phase Equil.* 19 (1998) 76–81.
- [23] F. Robert, P.-E. Lippens, J. Olivier-Fourcade, J.-C. Jumas, F. Gillot, M. Morcrette, J.-M. Tarascon, *J. Solid-State Chem.* 180 (2007) 339–348.
- [24] P.A. Flinn, in: G.K. Shenoy, F.E. Wagner (Eds.), *Mössbauer Isomer Shifts*, North-Holland Publishing Company, Amsterdam, New-York, Oxford, 1978, pp. 598–599.
- [25] J.-M. Themlin, M. Chtaib, L. Henrard, P. Lambin, J. Darville, J.-M. Gilles, *Phys. Rev. B* 46 (1992) 2460–2466.